JCTC Journal of Chemical Theory and Computation

pubs.acs.org/JCTC Article

Nano-Bio Interactions between DNA Nanocages and Human Serum Albumin

Dillon R. McCarthy, Jacob M. Remington, Jonathon B. Ferrell, Severin T. Schneebeli,* and Jianing Li*

Cite This: J. Chem. Theory Comput. 2023, 19, 7873−7881 Read Online

ACCESS | Metrics & More | Article Recommendations | Supporting Information

ABSTRACT: DNA nanostructures have emerged as promising nanomedical tools due to their biocompatibility and tunable behavior. Recent work has shown that DNA nanocages decorated with organic dendrimers strongly bind human serum albumin (HSA), yet the dynamic structures of these complexes remain uncharacterized. This theoretical and computational investigation elucidates the fuzzy interactions between dendritically functionalized cubic DNA nanocages and HSA. The dendrimer−HSA interactions occur via nonspecific binding with the protein thermodynamically and kinetically free to cross the open faces of the cubic scaffold. However, the rigidity of the DNA scaffold prevents the binding energetics from scaling with the number of dendrimers. These discoveries not only provide a useful framework by which to model general interactions of DNA nanostructures complexed with serum proteins but also give valuable molecular insight into the design of next-generation DNA nanomedicines.

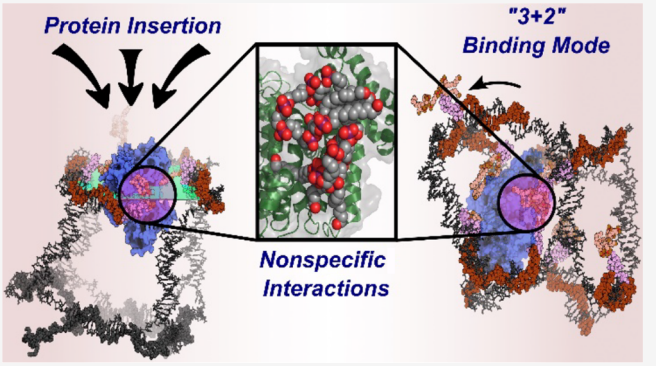

INTRODUCTION

Nanomedicines[1−6] utilizing DNA nanomaterials[7−17] (dimensions <100 nm; abbreviated DNs) have garnered significant attention due to their highly tunable biomolecular interactions. Predictable structural motifs, such as base pairs, hairpin loops, and G-quadruplexes, enable rational design of diverse and complex two- and three-dimensional topologies. DNs may also incorporate non-nucleic modifications[18] to further enhance their therapeutic effects.[19−25] Efforts in DNA nanomedicine span all stages of the therapeutic process,[26−31] especially in targeted drug delivery, serving as the therapeutic agent and/or as a nanocarrier.[32−38] DNs offer strategic advantages over non-nucleic nanotherapeutics, but improving their stability *in vivo* and *in vitro* is still crucial.[26,30,39−44] In particular, inhibiting enzymatic degradation of DNs by nuclease enzymes is a major challenge in developing practical DNA nanomedicines.[40,45,46]

Various strategies to protect DNs against enzymatic degradation have been discussed in the literature.[25,47−61] Obstruction of potential endonuclease and exonuclease binding through the formation of a protective shield represents one promising strategy[45] and has been successfully demonstrated using polyethylene glycol (PEG) and PEGylated polymers.[62−64] However, safety concerns regarding PEGylation are growing due to potential adverse effects, including hypersensitivity and accelerated blood clearance.[63,65−68] An emerging alternative is to conjugate DNs with serum proteins.[69−71] However, the design of viable nanostructure−protein conjugate pairs involves substantial trial and error, further complicated by difficulties in characterizing the complex nanoscale interactions. To rationally design DNs as nanomedicines, it is necessary to obtain a comprehensive understanding of their structural organization and interactions with relevant biomolecules.[41,72] Molecular modeling can close this gap by revealing how a DN's size, topology, and non-nucleic modifications impact key nano−bio interactions, which may be refined for greater stability, specificity, bioavailability, and immunogenicity. Elucidating these interactions at atomistic resolution will ultimately aid in translating DNA nanomedicines from *in vitro* to *in vivo* applications.

In this work, we studied the nano−bio interactions of DNA C_n nanocages ($n \in \{4,8\}$, the number of dendritic alkyl decorations) (Figure 1), first synthesized by Sleiman et al.[70] for the high-affinity association to human serum albumin (HSA). HSA is the most abundant protein in human blood (concentration 0.53−0.75 mM[73]) with a circulatory half-life of 19 days.[74] It is therefore used commonly to enhance the efficacy of small-molecule and nanomaterial therapeutics.[74−80] Seminal work from Sleiman et al. demonstrated that decoration of the C_n nanocages with dendritic alcohol-terminated alkyl chains (so-called D1 dendrimers) resulted in

Received: June 29, 2023
Revised: October 1, 2023
Accepted: October 3, 2023
Published: October 25, 2023

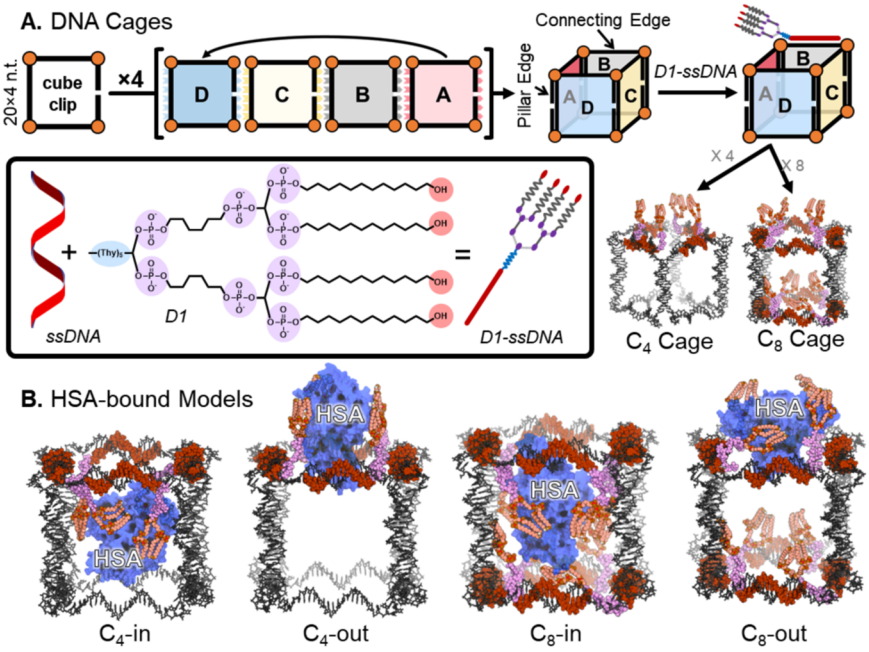

Figure 1. (A) Illustration of the DNA nanocage structures studied in this work. Each cage comprises four DNA strands or "cube clips", each containing 80 bases and four flexible linkers. Each side of the cage has 20 residues (~10 nm) linked consecutively by four thymine residues (shown as orange dots), while the 5′ and 3′ ends remain open. This produces a cage with four hybridized pillars, with eight single-stranded connecting edges on the top and bottom. The pillars are double stranded, while the single-stranded connecting edges become double stranded upon complementary D1-ssDNA binding. Hybridization of the D1-ssDNA strand to connecting edges of the cubic DNA cage scaffold creates a C_n cage, where C represents the cubic shape, and n is the number of hybridized D1-ssDNA on one (n = 4, C_4 cage) or two (n = 8, C_8 cage) faces. For the C_8 construct, all edges are hybridized, while only the top edges are hybridized for the C_4 construct, leaving the bottom edges unhybridized. (B) Initial models of the C_4 or C_8 cages in complex with HSA either in or out of the cage, constructed by DNA-BACon, our program to build atomistic models of DNA nanostructures (see SI for details). The HSA protein is colored lavender, ssDNA dark red, thymine linker light magenta, C and P atoms of D1 orange, and O atoms of D1 red. Nonpolar hydrogens have been omitted for clarity.

HSA binding at nanomolar affinity (K_d = 5−41 nM).[70] It was also shown that these DNA/HSA complexes possess enhanced stability in fetal bovine serum (FBS) compared to dendritic DNA (D1-ssDNA, Figure 1A) as reflected in an increase in the half-life from ~30 min to over 20 h. Unlike other nanomaterials known to form protein coronae,[81] these nanocages maintained a 1:1 binding ratio with HSA.[70] Increasing the number of dendrimers on the nanocage from four (named C_4) to eight (named C_8) leads to a small improvement in the K_d of the complexes but a significantly longer half-life.

RESULTS AND DISCUSSION

Maximized HSA−Dendrimer Contacts Are Found with the Protein in DNA Cages. Aided by DNA-BACon, our original program to build all-atom models of DNA nanostructures, we generated six models for C_4 and C_8 nanocages: three with HSA inside the cage (C_n-in) and three with HSA outside the cage (C_n-out). Each construct was simulated for 100 ns in SPC water with 15 mM Mg^{2+} and the number of Na^+ ions needed to neutralize the unit cell charge exactly. To analyze the C_4 (Figure 2) and C_8 (Figure 3) simulations, we define one HSA−nanocage contact as the contact between the dendrimer (D1) and HSA within 4.5 Å (heavy-atom distance). Many D1−HSA contacts formed within 50 ns, consistent with the experimental affinity trends.[70] Our contact counts consider the final 20 ns of each trajectory, over which averages remained stable with fluctuations of ±10% (Figure S1).

The most significant difference between the C_4-in and C_4-out trajectories was the number of simultaneously bound D1 dendrimers. The C_4-out constructs have 2 to 3 dendrimers bound to HSA, while the C_4-in constructs have 3 to 4 (Figure 2A). Thus, although an individual bound dendrimer interacts similarly with HSA in both C_4-in and C_4-out trajectories (Figure 2A), 25% more total contacts form between HSA and dendrimers in the C_4-in model than in the C_4-out model. This distinction was also observed when comparing the C_8-in and C_8-out trajectories (Figure 3). As one might expect from these contact counts, additional C_4 simulations (discussed below) suggest that the complexes with HSA inside the cage have slightly lower free energy than complexes in which HSA resides outside the cage.

Next, C_4 models were compared to C_8 models. In our simulations, despite all eight D1 dendrimers initially being positioned to encourage interaction with HSA in the C_8-in constructs (Figure 3B), no more than five dendrimers are bound at any time (Figure 3A). Moreover, we did not observe the simultaneous binding of four dendrimers from the same face of the nanocage in any C_8-in trajectory. This observation follows a "3 + 2" rule: at most, only three ligands from one face and two from the opposite face may be simultaneously bound.

In contrast to the C_8-in models, the C_4-in models supported binding of all four dendrimers from one face of the cage to HSA (Figure 2). To further investigate, we simulated a construct in which HSA was placed within a C_8 cage, but only four dendrimers from a single face were favorably positioned to encourage binding, while the other four dendrimers were

https://doi.org/10.1021/acs.jctc.3c00720
J. Chem. Theory Comput. 2023, 19, 7873−7881

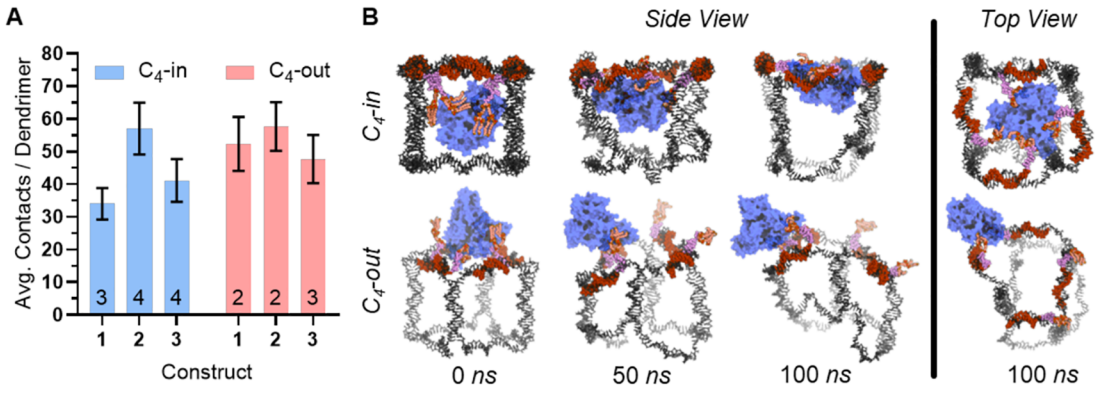

Figure 2. (A) Average number (±standard deviation) of contacts per bound dendrimer over the last 20 ns for all three C_4 cage systems. Three constructs with different HSA orientations were simulated for 100 ns for the C_4-in or C_4-out models. The contact analysis counts the contacts between D1 and HSA in the final 20 ns, using a heavy atom distance cutoff of 4.5 Å. Figure S13 illustrates our choice of cutoff distance. The inset value (at the bottom of each bar) represents the number of dendrimers bound (>1 contact) within the final 20 ns of the simulation. See Supporting Information for a description of the contact counting methods. (B) Snapshots at 0, 50, and 100 ns of two representative simulations. Solvent and counterions are hidden for clarity; representations are colored identically to Figure 1.

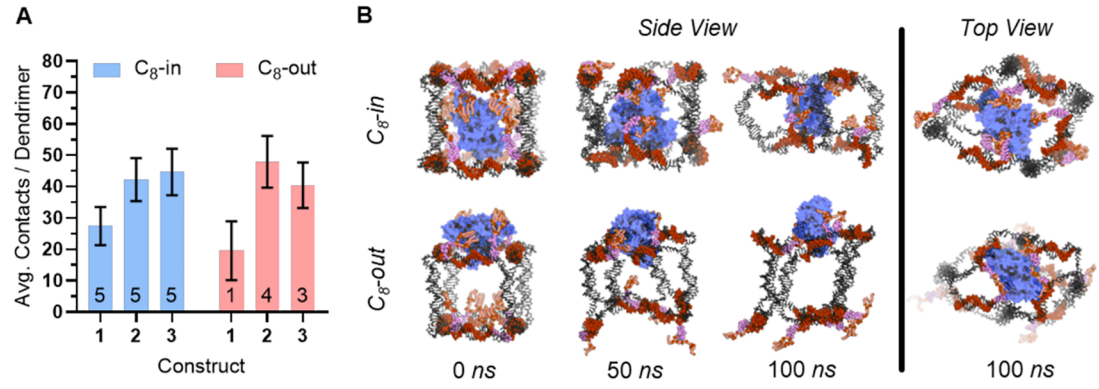

Figure 3. (A) Average number (±standard deviation) of contacts per bound dendrimer over the last 20 ns for all three constructs of the C_8 cage simulation. Three constructs with different HSA orientations were simulated for 100 ns for the C_8-in or C_8-out models. The contact analysis counts the contacts between D1 and HSA in the final 20 ns, using a heavy atom distance cutoff of 4.5 Å (same as Figure 2). The inset value represents the number of dendrimers bound (>1 contact) within the final 20 ns of the simulation. (B) Snapshots at 0, 50, and 100 ns of two representative simulations. Solvent and counterions are hidden for clarity.

pointed away from the center of the cage (Figures S2A). This model, named C_8-in*, is analogous to the C_4-in model except that its bottom face is fully hybridized with D1-ssDNA. Analysis of these simulations reveals a significantly decreased number of total interactions between the D1 dendrimers and HSA (Figure S2B), with no more than two dendrimers simultaneously bound. Thus, we propose that the "3 + 2" phenomenon arises, at least in part, from the greater energetic cost of deforming the more extensively hybridized C_8 DNA nanocages such that all four dendrimers from one face interact strongly with HSA, compared to the cost of deforming the partially single-stranded C_4 scaffolds.

HSA Protein in the DNA Cages Is Consistent with Experiments. The "3 + 2" model may explain the comparable experimental binding affinities between the differently functionalized DNA nanocages and HSA (K_d= 5 ± 2 nM for C_8 and K_d = 8 ± 2 nm for C_4).[70] To develop a semiquantitative model, we assume that each dendrimer in the nanocage binds independently to an HSA protein with an associated free energy ΔG_{lig}, while contributions to the free energy not resulting from the binding of ligands to HSA (including those from the conformational fluctuation of the nanocage) are represented by ΔG_{cons}. Thus, the total free energy of binding, ΔG_{tot}, can be expressed as

$$\Delta G_{tot} = n\Delta G_{lig} + \Delta G_{cons} \quad (1)$$

where n represents the number of bound dendrimers. From the previously reported dissociation constant,[70] we calculated binding free energies (ΔG_{tot}) of C_1, C_2, and C_4 cages as −9.6, −10.3, and −11.2 kcal/mol, respectively, via eq 2

$$\Delta G_{tot} = RT\ln(K_d) \quad (2)$$

where RT was chosen as 0.6 kcal/mol. Linear regression (r^2 = 0.99) sets the ΔG_{lig} and ΔG_{cons} values to −0.5 and −9.2 kcal/mol, respectively (Figure S3). Although intuition suggests that a negatively charged protein moving toward a negatively charged nanostructure without establishing significant contacts (n = 0) should not have such a favorable $\Delta G_{tot} = \Delta G_{cons}$, the linear model is a strong approximation for the more complex negative cooperative effects that may arise when two or more dendrimers are bound (Figure S3). In the case of the C_8 cage model (K_d = 5 nM,[70] ΔG_{tot} = −11.5 kcal/mol), the number of bound ligands n equals 4.6, consistent with our observation

https://doi.org/10.1021/acs.jctc.3c00720
J. Chem. Theory Comput. 2023, 19, 7873−7881

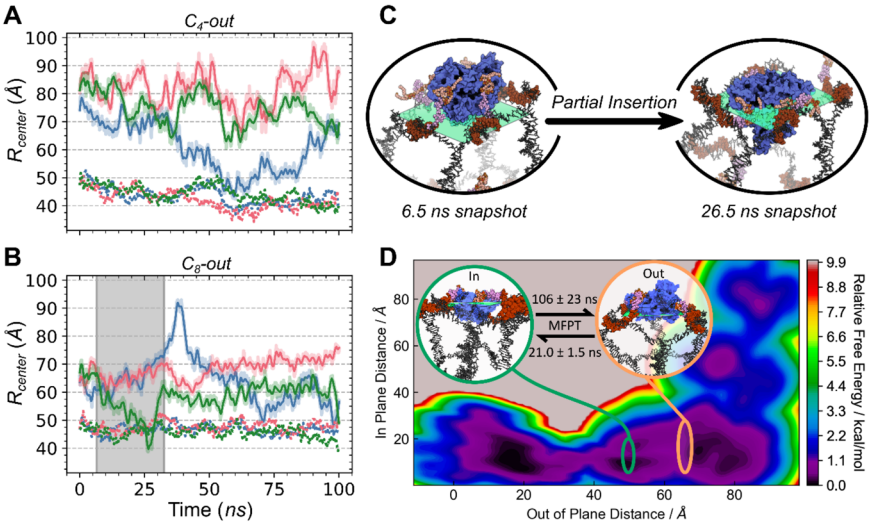

Figure 4. Displacements between HSA (solid trace) and the top face of the DNA cage (dotted trace) to the center of the DNA cage for all three C_4-out (A) and C_8-out (B) simulations. The displacements were calculated using the projected vectors as described in the Methods and Models section. The highlighted region of panel B ranges from 7 to 33 ns and highlights the partial insertion into the center of the cage and subsequent rapid outward diffusion of HSA. (C) Partial crossing and insertion of HSA into the center of the C_8 cage as highlighted by the gray region in panel B, solid green trace. The snapshot on the right highlights the point at which HSA has the smallest value of R_{center} at 26.5 ns. (D) Relative free energy surface for the C_4 cage was formed from combining C_4-in, C_4-out, and additional C_4 trajectories used to estimate a Markov state model near the transition region for HSA insertion ($R_{center} \sim 55$ Å). R_{face} is the displacement of the protein from the center of the top face of the cage projected into the plane of the top face of the cage. Also shown are atomistic structures from two regions (C_4-in as green and C_4-out as orange) used for the mean first passage time (MFPT) estimation. Similar energetics are shown for both the C_4-in and C_4-out models with slow crossing MFPTs. Errors in the MFPTs were estimated through Bayesian sampling with 500 samples.

that no more than five dendrimers could firmly bind to HSA in the C_8-in simulations.

We also observed slight variations in the contact count between the C_4 and C_8 cage models. When either three or four D1 dendrimers were bound to HSA in the C_4-in model, an average of 44 contacts per dendrimer were formed (Figure 2A). Comparatively, C_8-in shows an average of 38 contacts/dendrimer (Figure 3A), which represents a decrease of 15%. Considering the time-average of all dendrimer contacts, the C_8-out model had 53% fewer contacts than the C_4-out model. This difference between the C_4 and C_8 cage models may reflect differences in cage rigidity due to different hybridization. Still, more work is needed to fully characterize the complex responses of DNA nanocages to varying hybridization. A maximum number of possible contacts limits interactions between the protein and dendrimer. Such key differences arise in the ability of the C_8-in model to incorporate an additional dendrimer over the C_4-in model.

Molecular Mechanism of Protein Enclosure in DNA Cages. Next, considering the comparable sizes of HSA and our DNA nanocages, we investigated the mechanism of protein internalization. First, we define R_{center} as the displacement of HSA to the geometric cage center (Supporting Information). Analysis of the C_4-in simulations reveals that the protein may move from the center of the cage toward a dendrimer-functionalized face, while in the C_4-out and C_8-out simulations, the protein occasionally approaches the same face from the opposite direction (Figures 4A and B). Additionally, examination of the C_8-out simulations revealed a transient crossing event (Figure 4B, green trace). Initially, the R_{center} of HSA remained high (~65 Å at 6.5 ns, Figure 4C), indicating externally bound HSA. After approximately 20 ns of simulation time, the value of R_{center} (40 Å at 26.6 ns, Figure 4C) indicated that HSA had transiently crossed the face of the DNA nanocage) with, notably, only three dendrimers bound to the protein. Moreover, two "pillars" of the cage (P2 and P3) bent to accommodate the protein (Figure S5). Thus, cage dynamics and deformation can play roles in protein recognition and the formation of stable complexes.

To further verify our findings from the C_8 nanocages, we carried out swarm-based MD simulations of the C_4 models, which allowed for a more extensive sampling of the protein internalization process. Guided by the relative position of HSA to the DNA cage center, 10 "generations" of five replicas were successfully performed to sample the protein entering the cage. Simulations initialized with HSA at the center of the cage and totaling 0.4 μs were used to construct a Markov state model (MSM) (Figure 4D, Supporting Information). The relative free energy surface (FES), computed using the long-time equilibrium probability distribution of the MSM, was also used to unify the C_4-in and C_4-out simulation data (Figure 4D). The resultant FES shows that both C_4-in and C_4-out models have similar free energy with a low transition barrier in the parameter R_{center}, which roughly spans 50−70 Å. A mean first passage time (MFPT) analysis was used to explore the time scale for crossing this transition region, revealing that insertion events can occur as fast as 21.0 ± 1.5 ns, a time scale in good agreement with the single crossing event observed in the C_8-out models (Figure 4B and C). Transitions from the center to the outside of the cage can occur as fast as 106 ± 23 ns. Taken together, our data support a dynamic mechanism for HSA−DNA nanocage interactions, where HSA is capable of transitioning both into and out of the cage. The internalization of HSA into the DNA nanocages takes advantage of the intrinsic dynamics of the nanocage, which suggests that tuning these dynamics via rational design can modulate the nano−bio interactions with HSA.

https://doi.org/10.1021/acs.jctc.3c00720
J. Chem. Theory Comput. 2023, 19, 7873−7881

Fuzzy Nano−Bio interactions. Lastly, we systematically analyzed the specificity of the predominant D1−HSA nano−bio interactions (Supporting Information). Our search for specific interactions did not identify preferential binding of the dendrimers to any of the known small-molecule binding sites.[82−85] Examination of the binding frequencies in all four constructs revealed that only five residues are conserved. We also observed that contacts across all simulations are widely distributed (Figures S12 and S13), which further supports nonspecific interactions between the DNA nanocages and HSA.

Like proteins in fuzzy complexes,[86,87] these dendrimers were highly dynamic and adopted various conformations in our simulations, presumably due to their amphiphilic nature and structural flexibility. For example, extended conformations (Figure S10D1) allowed the terminal $-(CH_2)_{12}-OH$ groups to recognize the pockets where hydrophobic small molecules often bind. The folded conformations (Figure S10D2), which tightly pack the 12-carbon chains, formed a surface that interacts with the hydrophobic patches of HSA. This state likely enhanced the interactions of the amphipathic dendrimer with the protein and distinguished itself from poly-(amidoamines) (PAMAM) dendrimers,[88,89] which form weak complexes with HSA. The ambiguity in the D1 dendrimer binding to the HSA surface contrasts with the specific/selective binding between proteins and small-molecule ligands.

CONCLUSIONS

In this work, we computationally studied prototypical DNA nanocages interacting with a serum protein, HSA, and gained novel insight into the molecular origin of the nano−bio interactions. We discovered that DNA nanocages recognize HSA mainly through nonspecific or fuzzy interactions between their dendrimer decorations and the protein. We also identified several unique features (i.e., the number of dendrimers, cage rigidity, and protein positioning) in the design of DNA nanocages that contribute to the high affinity and the 1:1 binding stoichiometry. While internalization of HSA is optimal for maximizing contacts with the dendrimer, the protein position is different between each construct. In the C_8 cage, HSA remains centrally located for the duration of the simulation, while in the C_4 cage, the protein prefers a position at or near the decorated face. Further computational and experimental studies are still needed to explain the complex's protection mechanism to extend the DNA's half-life, because many other proteins in serum, such as the nucleases and the neonatal Fc receptor, may be involved. Although DNA has been studied as a highly programmable material,[90−93] our research shows the potential of molecular modeling and simulation to bridge the gap from the design to the expected properties. Ultimately, this work provides the first in-depth investigation of the nano−bio interactions between DNA nanomaterials and a human serum protein. Building on the discussed methodology, we are ready to construct an *in silico* platform to design and select new DNA nanocages and potent protein partners or targets toward nanomedicines.

METHODS AND MODELS

Model Construction. We have developed an in-house software program, DNA Build Assemble CONstruct, (DNA-BACon) to construct precisely and efficiently three-dimensional (3D) atomistic models of DNA nanocages for all-atom modeling. In this work, we used DNA-BACon to construct the C_4 and C_8 cage models (Figure 1). Our input files for DNA-BACon that describe the sequences of DNA from and the thymine linkers to connect the corners are provided in a GitHub repository (https://github.com/ftclark3/DNA-BACon). The thymine linker PDB was generated using Maestro (Schrödinger, Inc.). With the C_4 and C_8 cage models, we further built the HSA−DNA nanocage complexes in Maestro. We used the Protein Preparation Wizard (Maestro) to prepare the HSA protein model (PDB ID: 1AO6), which was then placed either inside or outside of the nanocages in three indiscriminate spatial and rotational orientations, leading to 12 constructs (three constructs for C_4-out, C_4-in, C_8-out, and C_8-in, Figure 1B). To promote dendrimer interaction with the protein, the dendrimers were preorganized around the protein using Maestro's atom sculpting before being relaxed to generate initial solute positions. All constructs were minimized in Maestro to eliminate steric clashes. Finally, all constructs were solvated with the SPC water model (15 Å cubic buffer) using the System Builder program in Maestro. Mg^{2+} ions were then added to achieve a concentration of 15 mM to mimic the experimental condition, while the remaining negative charge of the complex was neutralized with Na^+ counterions.

MD Simulation Setup. A summary of our simulations (totaling 2 μs) is provided in Table S2. The system size was around 374,000−890,000 atoms in each construct. All simulations used the OPLS3e force field[94,95] and were run in the Desmond (Schrödinger, Inc.) on GPUs. Each construct went through a multistage equilibration and a 100 ns MD production run in the NPT ensemble (300 K, 1 bar, Nosé−Hoover thermostat with 1-ps relaxation time, and Martyna−Tobias−Klein isotropic barostat with 2 ps relaxation time) using a 2-fs time step. The particle mesh Ewald (PME) technique was used for the electrostatic calculations. A van der Waals and short-range electrostatic cutoff of 9 Å was selected and updated with a time step of 2 fs, while long-range electrostatics were calculated every 6 fs. One simulation was run for each construct.

MD Simulation Analysis. Visualization was performed using VMD1.9.3 and Pymol. Our MD analysis was performed using in-house Tcl and Python scripts. Trajectories were unwrapped and aligned to the initial frame of each simulation before analysis and visually checked using VMD. To determine an appropriate cutoff distance for D1/HSA interactions, histograms of the interaction count between D1 and HSA with a spacing of 0.25 Å were measured (Figure S13) to capture the important atom pairs in all simulations. In our simulations, a heavy-atom−heavy-atom distance of 4.5 Å captured approximately 50% of the interactions and was therefore chosen as our cutoff distance. To determine the area percentage of the protein's surface involved in interactions with the D1 dendrimers, VMD's atom selection language was utilized to selectively evaluate the solvent-accessible surface area (SASA) for those HSA atoms within 4.5 Å of the dendrimer and then compared with the SASA of the HSA protein. Due to the highly dynamic nature of these systems, only the last 20 ns of all constructs were analyzed, as this typically provided a consistent window by which to compare all simulations.

Swarm Simulations Setup. Initially, five conformationally unique structures were chosen from our unbiased C_4-in simulations. Next, all five replicas were prepared, parametrized as described above, and simulated for 10 ns. Next, the value

https://doi.org/10.1021/acs.jctc.3c00720
J. Chem. Theory Comput. 2023, 19, 7873−7881

R_{center} (see below) was calculated for all five replicas. Then, a new set of five unique structures were chosen such that the value of R_{center} had increased—indicating movement of HSA away from the center of the cage, and simulated for 10 ns as before. If five structures did not exist where R_{center} did not increase (in other words, the protein did not move away from the center of the cage) could not be found when $t > 0$, the simulations were restarted and assigned a new seed. A second parameter, R_{face}, was defined as the magnitude of the projection of the vector from the geometric center of the cage to the geometric center of HSA, $\vec{V}_{HSA}$, onto the plane defined by the decorated C_4 cage face. (This plane is analogous to that shown in green in Figure 4C.) To ensure HSA remained oriented along a reasonable trajectory path, all structures with $R_{face} > 30$ Å were disqualified and substituted for the next best structure which met our R_{center} selection criteria. This process was repeated until additional simulations did not increase the R_{center} after multiple attempts. In this work, 10 "generations" of five replicas were successful until the value of R_{center} no longer increased. The resulting trajectories were then used to construct a Markov state model (MSM) using PyEMMA[96] as described in the Supporting Information. These swarm simulations were entirely automated and designed to work with Desmond MD; the code is available as a GitHub repository upon request.

To measure the displacement, R_{center}, of HSA from the center of the DNA nanocage, we utilized eq 3 as described below:

$$R_{center} = \hat{V}_T \bullet \vec{V}_{HSA} \tag{3}$$

where $\hat{V}_T$ is the unit vector between the geometric center and top face of the nanocage, and $\vec{V}_{HSA}$ is the vector between the geometric center of the nanocage and geometric center of HSA (Figure S14). Here, the top face of the nanocage is defined uniformly in all constructs to ensure consistency. Equation 3 is used to minimize changes in displacement associated with the translation of the protein in the same plane as the top face of the DNA nanocage.

The pitch of each pillar, θ_p, is described in eq 4 as

$$\theta_p = \cos^{-1}\left(\frac{\vec{V}_i \bullet \vec{V}_T}{\|\vec{V}_i\| \bullet \|\vec{V}_T\|}\right) \tag{4}$$

where $\vec{V}_i$ is a vector drawn from the midpoint of each main pillar to the top corner of the DNA nanocage, and $\vec{V}_T$ is the vector between the geometric center and top face of the nanocage (see Figure S14 for more detail). In all models, the "top face" of the cage was consistently defined to be the same four strands to avoid ambiguity. A depiction of all four pillars is shown in Figure S5A.

Markov State Model Estimation. Following an initial relaxation of the swarm MD simulations (first two iterations totaling 100 ns), in-plane and out-of-plane HSA distances for the remaining 40 distinct 10-ns trajectories were used as collective variables for MSM estimation within PyEMMA. *K*-means clustering using 50 centers initially discretized the trajectory state space (Figure S6A). Implied time scale plots were used to select a 1-ns lag time for estimating MSMs (Figure S6B). At lag times longer than 1 ns, the relaxation time scales of the computed MSMs were constant. Multiple, 500, MSMs were then computed using Bayesian sampling to enable reporting of statistical quantities. First, we visualized the slowest kinetic process in the input collective variable space, revealing positive and negative amplitudes on either side of the out-of-plane HSA distance coordinate near the face of the DNA cage containing the ligated therapeutic DNA (Figure S7). This demonstrates that the resultant MSM captures the difficult-to-sample transitions between C_4-in and C4-out models. Mean first passage time (MFPTs) and their standard deviations between the C_4-in and C_4-out models in the sampled trajectories were estimated by classifying microstates as -in or -out using cutoffs of distance < 50 Å and distance > 65 Å, respectively. Free energy surfaces (FES) were then computed from the MSM model by using a weighted kernel density estimation (KDE) of the long-time equilibrium distribution of the MSM (Figure S9B). In addition, KDE was also used for computing the FES from the C_4-in and C_4-out simulations (Figure S8A and C). To combine the three FES in Figure S8 into the FES (Figure 4), we used nonlinear optimization of the unknown energy shift (s_{alt}) to minimize the average absolute difference in energy (ADE) surface values in overlapping regions (eq 5).

$$\mathrm{ADE}(s_{alt}) = \frac{1}{N_{xy}} \sum_{x,y} |\mathrm{FES}_{in}(x, y) - \mathrm{FES}_{alt}(x, y) + s_{alt}| \tag{5}$$

In eq 5, N_{xy} are the number of grid points in the overlapping regions between FES from C_4-in simulations (FES_{in}) and FES from C_4-out or C_4-msm simulations (FES_{alt}) (alt meaning "out" or msm). Values of the ADE and shift are shown in Figure S9 using overlapping regions of 45 Å < out-of-plane distance ≤ 50 Å for FES_{msm} and 58 Å < out-of-plane distance ≤ 63 Å for FES_{out}.

■ ASSOCIATED CONTENT

Data Availability Statement

DNA-BACon is freely available for use and can be found at https://github.com/ftclark3/DNA-BACon. MD Trajectories are available upon request to the corresponding author. Code used for the swarm MD simulations and Markov state modeling can be accessed free of charge at https://github.com/dillonrmccarthy/hsa-swarm-msm-2022.

Supporting Information

Simulation parameters including the base-pair sequence of all nanocage models. These sequences can be used for DNA-BACon to reconstruct the model systems. Experimental details and analysis of fragment docking experiments, and analysis of additional dendrimer/protein interactions, and corresponding figures for the Markov state modeling. The Supporting Information is available free of charge at https://pubs.acs.org/doi/10.1021/acs.jctc.3c00720.

(PDF)

■ AUTHOR INFORMATION

Corresponding Authors

Severin T. Schneebeli − *Department of Chemistry, University of Vermont, Burlington, Vermont 05405, United States; Department of Industrial and Molecular Pharmaceutics and Department of Chemistry, Purdue University, West Lafayette, Indiana 47907, United States;* orcid.org/0000-0002-9511-9922; Email: schneebeli@purdue.edu

Jianing Li − *Department of Chemistry, University of Vermont, Burlington, Vermont 05405, United States; Borch Department of Medicinal Chemistry and Molecular Pharmacology, Purdue University, West Lafayette, Indiana*

https://doi.org/10.1021/acs.jctc.3c00720
J. Chem. Theory Comput. 2023, 19, 7873−7881

47907, United States; orcid.org/0000-0002-0143-8894; Email: jianing-li@purdue.edu

Authors

Dillon R. McCarthy − *Department of Chemistry, University of Vermont, Burlington, Vermont 05405, United States*

Jacob M. Remington − *Department of Chemistry, University of Vermont, Burlington, Vermont 05405, United States*

Jonathon B. Ferrell − *Department of Chemistry, University of Vermont, Burlington, Vermont 05405, United States*

Complete contact information is available at: https://pubs.acs.org/10.1021/acs.jctc.3c00720

Notes

The authors declare no competing financial interest.

■ ACKNOWLEDGMENTS

We thank Prof. H. Sleiman (McGill) and Dr. A. Lacroix (McGill) for helpful and enlightening discussions. The initial unbiased MD work was supported by the National Science Foundation (Grants CHE-1848444/2317652 to S.T.S. and CHE-1945394 to J.L.), while the Markov State modeling work was supported by the NIH (R35GM147579 to S.T.S.).

■ REFERENCES

(1) Chen, G.; Roy, I.; Yang, C.; Prasad, P. N. Nanochemistry and Nanomedicine for Nanoparticle-Based Diagnostics and Therapy. *Chem. Rev.* **2016**, *116* (5), 2826−2885.

(2) Moghimi, S. M.; Hunter, A. C.; Murray, J. C. Nanomedicine: Current Status and Future Prospects. *FASEB J.* **2005**, *19* (3), 311−330.

(3) Pelaz, B.; Alexiou, C.; Alvarez-Puebla, R. A.; Alves, F.; Andrews, A. M.; Ashraf, S.; Balogh, L. P.; Ballerini, L.; Bestetti, A.; Brendel, C.; Bosi, S.; Carril, M.; Chan, W. C. W.; Chen, C.; Chen, X.; Chen, X.; Cheng, Z.; Cui, D.; Du, J.; Dullin, C.; Escudero, A.; Feliu, N.; Gao, M.; George, M.; Gogotsi, Y.; Grünweller, A.; Gu, Z.; Halas, N. J.; Hampp, N.; Hartmann, R. K.; Hersam, M. C.; Hunziker, P.; Jian, J.; Jiang, X.; Jungebluth, P.; Kadhiresan, P.; Kataoka, K.; Khademhosseini, A.; Kopeček, J.; Kotov, N. A.; Krug, H. F.; Lee, D. S.; Lehr, C.-M.; Leong, K. W.; Liang, X.-J.; Ling Lim, M.; Liz-Marzán, L. M.; Ma, X.; Macchiarini, P.; Meng, H.; Möhwald, H.; Mulvaney, P.; Nel, A. E.; Nie, S.; Nordlander, P.; Okano, T.; Oliveira, J.; Park, T. H.; Penner, R. M.; Prato, M.; Puntes, V.; Rotello, V. M.; Samarakoon, A.; Schaak, R. E.; Shen, Y.; Sjöqvist, S.; Skirtach, A. G.; Soliman, M. G.; Stevens, M. M.; Sung, H.-W.; Tang, B. Z.; Tietze, R.; Udugama, B. N.; VanEpps, J. S.; Weil, T.; Weiss, P. S.; Willner, I.; Wu, Y.; Yang, L.; Yue, Z.; Zhang, Q.; Zhang, Q.; Zhang, X.-E.; Zhao, Y.; Zhou, X.; Parak, W. J. Diverse Applications of Nanomedicine. *ACS Nano* **2017**, *11* (3), 2313−2381.

(4) Prasad, M.; Lambe, U. P.; Brar, B.; Shah, I.; J, M.; Ranjan, K.; Rao, R.; Kumar, S.; Mahant, S.; Khurana, S. K.; Iqbal, H. M. N.; Dhama, K.; Misri, J.; Prasad, G. Nanotherapeutics: An Insight into Healthcare and Multi-Dimensional Applications in Medical Sector of the Modern World. *Biomed. Pharmacother.* **2018**, *97*, 1521−1537.

(5) Soares, S.; Sousa, J.; Pais, A.; Vitorino, C. Nanomedicine: Principles, Properties, and Regulatory Issues. *Front. Chem.* **2018**, *6*, 360.

(6) Ventola, C. L. The Nanomedicine Revolution. *P. T.* **2012**, *37* (9), 512−525.

(7) Dey, S.; Fan, C.; Gothelf, K. V.; Li, J.; Lin, C.; Liu, L.; Liu, N.; Nijenhuis, M. A. D.; Saccà, B.; Simmel, F. C.; Yan, H.; Zhan, P. DNA Origami. *Nat. Rev. Methods Primers* **2021**, *1* (1), 1−24.

(8) Hong, F.; Zhang, F.; Liu, Y.; Yan, H. DNA Origami: Scaffolds for Creating Higher Order Structures. *Chem. Rev.* **2017**, *117* (20), 12584−12640.

(9) Ji, J.; Karna, D.; Mao, H. DNA Origami Nano-Mechanics. *Chem. Soc. Rev.* **2021**, *50* (21), 11966−11978.

(10) Lu, C.-H.; Willner, B.; Willner, I. DNA Nanotechnology: From Sensing and DNA Machines to Drug-Delivery Systems. *ACS Nano* **2013**, *7* (10), 8320−8332.

(11) Nummelin, S.; Kommeri, J.; Kostiainen, M. A.; Linko, V. Evolution of Structural DNA Nanotechnology. *Adv. Mater.* **2018**, *30* (24), No. 1703721.

(12) Pinheiro, A. V.; Han, D.; Shih, W. M.; Yan, H. Challenges and Opportunities for Structural DNA Nanotechnology. *Nat. Nanotechnol.* **2011**, *6* (12), 763−772.

(13) Seeman, N. C. An Overview of Structural DNA Nanotechnology. *Mol. Biotechnol* **2007**, *37* (3), 246.

(14) Seeman, N. C.; Sleiman, H. F. DNA Nanotechnology. *Nat. Rev. Mater.* **2018**, *3* (1), 1−23.

(15) Tapio, K.; Bald, I. The Potential of DNA Origami to Build Multifunctional Materials. *Multifunct. Mater.* **2020**, *3* (3), No. 032001.

(16) Wang, P.; Meyer, T. A.; Pan, V.; Dutta, P. K.; Ke, Y. The Beauty and Utility of DNA Origami. *Chem.* **2017**, *2* (3), 359−382.

(17) Zhang, F.; Nangreave, J.; Liu, Y.; Yan, H. Structural DNA Nanotechnology: State of the Art and Future Perspective. *J. Am. Chem. Soc.* **2014**, *136* (32), 11198−11211.

(18) Madsen, M.; Gothelf, K. V. Chemistries for DNA Nanotechnology. *Chem. Rev.* **2019**, *119* (10), 6384−6458.

(19) Chandrasekaran, A. R.; MacIsaac, M.; Vilcapoma, J.; Hansen, C. H.; Yang, D.; Wong, W. P.; Halvorsen, K. DNA Nanoswitch Barcodes for Multiplexed Biomarker Profiling. *Nano Lett.* **2021**, *21* (1), 469−475.

(20) Joaqui-Joaqui, M. A.; Maxwell, Z.; Ramakrishnam Raju, M. V.; Jiang, M.; Srivastava, K.; Shao, F.; Arriaga, E. A.; Pierre, V. C. Metallointercalators-DNA Tetrahedron Supramolecular Self-Assemblies with Increased Serum Stability. *ACS Nano* **2022**, *16* (2), 2928−2941.

(21) Knappe, G. A.; Wamhoff, E.-C.; Read, B. J.; Irvine, D. J.; Bathe, M. In Situ Covalent Functionalization of DNA Origami Virus-like Particles. *ACS Nano* **2021**, *15* (9), 14316−14322.

(22) Märcher, A.; Nijenhuis, M. A. D.; Gothelf, K. V. A Wireframe DNA Cube: Antibody Conjugate for Targeted Delivery of Multiple Copies of Monomethyl Auristatin E. *Angew. Chem., Int. Ed.* **2021**, *60* (40), 21691−21696.

(23) Modi, S.; M G, S.; Goswami, D.; Gupta, G. D.; Mayor, S.; Krishnan, Y. A DNA Nanomachine That Maps Spatial and Temporal PH Changes inside Living Cells. *Nat. Nanotechnol.* **2009**, *4* (5), 325−330.

(24) Pal, S.; Rakshit, T. Folate-Functionalized DNA Origami for Targeted Delivery of Doxorubicin to Triple-Negative Breast Cancer. *Frontiers in Chemistry* **2021**, *9*, 721105.

(25) Wamhoff, E.-C.; Romanov, A.; Huang, H.; Read, B. J.; Ginsburg, E.; Knappe, G. A.; Kim, H. M.; Farrell, N. P.; Irvine, D. J.; Bathe, M. Controlling Nuclease Degradation of Wireframe DNA Origami with Minor Groove Binders. *ACS Nano* **2022**, *16*, 8954.

(26) Bujold, K. E.; Lacroix, A.; Sleiman, H. F. DNA Nanostructures at the Interface with Biology. *Chem.* **2018**, *4* (3), 495−521.

(27) Campolongo, M. J.; Tan, S. J.; Xu, J.; Luo, D. DNA Nanomedicine: Engineering DNA as a Polymer for Therapeutic and Diagnostic Applications. *Adv. Drug. Delivery Rev.* **2010**, *62* (6), 606−616.

(28) Chakraborty, A.; Ravi, S. P.; Shamiya, Y.; Cui, C.; Paul, A. Harnessing the Physicochemical Properties of DNA as a Multifunctional Biomaterial for Biomedical and Other Applications. *Chem. Soc. Rev.* **2021**, *50* (13), 7779−7819.

(29) Henry, S. J. W.; Stephanopoulos, N. Functionalizing DNA Nanostructures for Therapeutic Applications. *WIREs Nanomedicine and Nanobiotechnology* **2021**, *13* (6), No. e1729.

(30) Ma, W.; Zhan, Y.; Zhang, Y.; Mao, C.; Xie, X.; Lin, Y. The Biological Applications of DNA Nanomaterials: Current Challenges and Future Directions. *Sig Transduct Target Ther* **2021**, *6* (1), 1−28.

(31) Zhang, Y.; Tu, J.; Wang, D.; Zhu, H.; Maity, S. K.; Qu, X.; Bogaert, B.; Pei, H.; Zhang, H. Programmable and Multifunctional

DNA-Based Materials for Biomedical Applications. *Adv. Mater.* **2018**, *30* (24), No. 1703658.
(32) Chi, Q.; Yang, Z.; Xu, K.; Wang, C.; Liang, H. DNA Nanostructure as an Efficient Drug Delivery Platform for Immunotherapy. *Frontiers in Pharmacology* **2020**, *10*, 1585.
(33) Hu, Q.; Li, H.; Wang, L.; Gu, H.; Fan, C. DNA Nanotechnology-Enabled Drug Delivery Systems. *Chem. Rev.* **2019**, *119* (10), 6459−6506.
(34) Lee, H.; Lytton-Jean, A. K. R.; Chen, Y.; Love, K. T.; Park, A. I.; Karagiannis, E. D.; Sehgal, A.; Querbes, W.; Zurenko, C. S.; Jayaraman, M.; Peng, C. G.; Charisse, K.; Borodovsky, A.; Manoharan, M.; Donahoe, J. S.; Truelove, J.; Nahrendorf, M.; Langer, R.; Anderson, D. G. Molecularly Self-Assembled Nucleic Acid Nanoparticles for Targeted in Vivo SiRNA Delivery. *Nat. Nanotechnol.* **2012**, *7* (6), 389−393.
(35) Madhanagopal, B. R.; Zhang, S.; Demirel, E.; Wady, H.; Chandrasekaran, A. R. DNA Nanocarriers: Programmed to Deliver. *Trends Biochem. Sci.* **2018**, *43* (12), 997−1013.
(36) Schüller, V. J.; Heidegger, S.; Sandholzer, N.; Nickels, P. C.; Suhartha, N. A.; Endres, S.; Bourquin, C.; Liedl, T. Cellular Immunostimulation by CpG-Sequence-Coated DNA Origami Structures. *ACS Nano* **2011**, *5* (12), 9696−9702.
(37) Stewart, J. M.; Viard, M.; Subramanian, H. K. K.; Roark, B. K.; Afonin, K. A.; Franco, E. Programmable RNA Microstructures for Coordinated Delivery of SiRNAs. *Nanoscale* **2016**, *8* (40), 17542−17550.
(38) Weiden, J.; Bastings, M. M. C. DNA Origami Nanostructures for Controlled Therapeutic Drug Delivery. *Curr. Opin. Colloid Interface Sci.* **2021**, *52*, No. 101411.
(39) Afonin, K. A.; Dobrovolskaia, M. A.; Ke, W.; Grodzinski, P.; Bathe, M. Critical Review of Nucleic Acid Nanotechnology to Identify Gaps and Inform a Strategy for Accelerated Clinical Translation. *Adv. Drug Delivery Rev.* **2022**, *181*, No. 114081.
(40) Chandrasekaran, A. R. Nuclease Resistance of DNA Nanostructures. *Nat. Rev. Chem.* **2021**, *5* (4), 225−239.
(41) Green, C. M.; Mathur, D.; Medintz, I. L. Understanding the Fate of DNA Nanostructures inside the Cell. *J. Mater. Chem. B* **2020**, *8* (29), 6170−6178.
(42) Hahn, J.; Wickham, S. F. J.; Shih, W. M.; Perrault, S. D. Addressing the Instability of DNA Nanostructures in Tissue Culture. *ACS Nano* **2014**, *8* (9), 8765−8775.
(43) Keller, A.; Linko, V. Challenges and Perspectives of DNA Nanostructures in Biomedicine. *Angew. Chem., Int. Ed.* **2020**, *59* (37), 15818−15833.
(44) Lacroix, A.; Sleiman, H. F. DNA Nanostructures: Current Challenges and Opportunities for Cellular Delivery. *ACS Nano* **2021**, *15* (3), 3631−3645.
(45) Perrault, S. D.; Shih, W. M. Virus-Inspired Membrane Encapsulation of DNA Nanostructures To Achieve In Vivo Stability. *ACS Nano* **2014**, *8* (5), 5132−5140.
(46) Conway, J. W.; McLaughlin, C. K.; Castor, K. J.; Sleiman, H. DNA Nanostructure Serum Stability: Greater than the Sum of Its Parts. *Chem. Commun.* **2013**, *49* (12), 1172−1174.
(47) Chandrasekaran, A. R. Nuclease Resistance of DNA Nanostructures. *Nat. Rev. Chem.* **2021**, *5* (4), 225−239.
(48) Hahn, J.; Wickham, S. F. J.; Shih, W. M.; Perrault, S. D. Addressing the Instability of DNA Nanostructures in Tissue Culture. *ACS Nano* **2014**, *8* (9), 8765−8775.
(49) Agarwal, N. P.; Matthies, M.; Gür, F. N.; Osada, K.; Schmidt, T. L. Block Copolymer Micellization as a Protection Strategy for DNA Origami. *Angew. Chem., Int. Ed.* **2017**, *56* (20), 5460−5464.
(50) Goltry, S.; Hallstrom, N.; Clark, T.; Kuang, W.; Lee, J.; Jorcyk, C.; Knowlton, W. B.; Yurke, B.; Hughes, W. L.; Graugnard, E. DNA Topology Influences Molecular Machine Lifetime in Human Serum. *Nanoscale* **2015**, *7* (23), 10382−10390.
(51) Keum, J.-W.; Bermudez, H. Enhanced Resistance of DNAnanostructures to Enzymatic Digestion. *Chem. Commun.* **2009**, *45*, 7036−7038.
(52) Kim, Y.; Yin, P. Enhancing Biocompatible Stability of DNA Nanostructures Using Dendritic Oligonucleotides and Brick Motifs. *Angew. Chem., Int. Ed.* **2020**, *59* (2), 700−703.
(53) Ramakrishnan, S.; Schärfen, L.; Hunold, K.; Fricke, S.; Grundmeier, G.; Schlierf, M.; Keller, A.; Krainer, G. Enhancing the Stability of DNA Origami Nanostructures: Staple Strand Redesign versus Enzymatic Ligation. *Nanoscale* **2019**, *11* (35), 16270−16276.
(54) Henry, S. J. W.; Stephanopoulos, N. Functionalizing DNA Nanostructures for Therapeutic Applications. *WIREs Nanomedicine and Nanobiotechnology* **2021**, *13* (6), No. e1729.
(55) Anastassacos, F. M.; Zhao, Z.; Zeng, Y.; Shih, W. M. Glutaraldehyde Cross-Linking of Oligolysines Coating DNA Origami Greatly Reduces Susceptibility to Nuclease Degradation. *J. Am. Chem. Soc.* **2020**, *142* (7), 3311−3315.
(56) Ponnuswamy, N.; Bastings, M. M. C.; Nathwani, B.; Ryu, J. H.; Chou, L. Y. T.; Vinther, M.; Li, W. A.; Anastassacos, F. M.; Mooney, D. J.; Shih, W. M. Oligolysine-Based Coating Protects DNA Nanostructures from Low-Salt Denaturation and Nuclease Degradation. *Nat. Commun.* **2017**, *8* (1), 15654.
(57) Shaukat, A.; Anaya-Plaza, E.; Julin, S.; Linko, V.; Torres, T.; de la Escosura, A.; Kostiainen, M. A. Phthalocyanine−DNA Origami Complexes with Enhanced Stability and Optical Properties. *Chem. Commun.* **2020**, *56* (53), 7341−7344.
(58) Ahmadi, Y.; De Llano, E.; Barisic, I. (Poly)Cation-Induced Protection of Conventional and Wireframe DNA Origami Nanostructures. *Nanoscale* **2018**, *10* (16), 7494−7504.
(59) Auvinen, H.; Zhang, H.; Nonappa; Kopilow, A.; Niemelä, E. H.; Nummelin, S.; Correia, A.; Santos, H. A.; Linko, V.; Kostiainen, M. A. Protein Coating of DNA Nanostructures for Enhanced Stability and Immunocompatibility. *Adv. Healthcare Mater.* **2017**, *6* (18), No. 1700692.
(60) Chandrasekhar, S.; Prakash, P. S.; Schmidt, T.-L. Stability and Stabilization of DNA Nanostructures in Biomedical Applications. In *DNA Origami*; John Wiley & Sons, Ltd., 2022; pp 333−377. DOI: 10.1002/9781119682561.ch16.
(61) Li, Y.; Song, L.; Wang, B.; He, J.; Li, Y.; Deng, Z.; Mao, C. Universal PH-Responsive and Metal-Ion-Free Self-Assembly of DNA Nanostructures. *Angew. Chem., Int. Ed.* **2018**, *57* (23), 6892−6895.
(62) Ponnuswamy, N.; Bastings, M. M. C.; Nathwani, B.; Ryu, J. H.; Chou, L. Y. T.; Vinther, M.; Li, W. A.; Anastassacos, F. M.; Mooney, D. J.; Shih, W. M. Oligolysine-Based Coating Protects DNA Nanostructures from Low-Salt Denaturation and Nuclease Degradation. *Nat. Commun.* **2017**, *8* (1), 15654.
(63) Zorzi, A.; Middendorp, S. J.; Wilbs, J.; Deyle, K.; Heinis, C. Acylated Heptapeptide Binds Albumin with High Affinity and Application as Tag Furnishes Long-Acting Peptides. *Nat. Commun.* **2017**, *8* (1), 16092.
(64) Anastassacos, F. M.; Zhao, Z.; Zeng, Y.; Shih, W. M. Glutaraldehyde Cross-Linking of Oligolysines Coating DNA Origami Greatly Reduces Susceptibility to Nuclease Degradation. *J. Am. Chem. Soc.* **2020**, *142* (7), 3311−3315.
(65) Chanan-Khan, A.; Szebeni, J.; Savay, S.; Liebes, L.; Rafique, N. M.; Alving, C. R.; Muggia, F. M. Complement Activation Following First Exposure to Pegylated Liposomal Doxorubicin (Doxil®): Possible Role in Hypersensitivity Reactions. *Annals of Oncology* **2003**, *14* (9), 1430−1437.
(66) Knop, K.; Hoogenboom, R.; Fischer, D.; Schubert, U. S. Poly(Ethylene Glycol) in Drug Delivery: Pros and Cons as Well as Potential Alternatives. *Angew. Chem., Int. Ed.* **2010**, *49* (36), 6288−6308.
(67) Schellekens, H.; Hennink, W. E.; Brinks, V. The Immunogenicity of Polyethylene Glycol: Facts and Fiction. *Pharm. Res.* **2013**, *30* (7), 1729−1734.
(68) van Witteloostuijn, S. B.; Pedersen, S. L.; Jensen, K. J. Half-Life Extension of Biopharmaceuticals Using Chemical Methods: Alternatives to PEGylation. *ChemMedChem.* **2016**, *11* (22), 2474−2495.
(69) Auvinen, H.; Zhang, H.; Nonappa; Kopilow, A.; Niemelä, E. H.; Nummelin, S.; Correia, A.; Santos, H. A.; Linko, V.; Kostiainen, M. A. Protein Coating of DNA Nanostructures for Enhanced Stability

and Immunocompatibility. *Adv. Healthcare Mater.* **2017**, *6* (18), No. 1700692.
(70) Lacroix, A.; Edwardson, T. G. W.; Hancock, M. A.; Dore, M. D.; Sleiman, H. F. Development of DNA Nanostructures for High-Affinity Binding to Human Serum Albumin. *J. Am. Chem. Soc.* **2017**, *139* (21), 7355−7362.
(71) Li, X.; Xu, F.; Yang, D.; Wang, P. A DNA-Binding, Albumin-Targeting Fusion Protein Promotes the Cellular Uptake and Bioavailability of Framework DNA Nanostructures. *Nanoscale* **2021**, *13* (12), 6038−6042.
(72) Raniolo, S.; Croce, S.; Thomsen, R. P.; Okholm, A. H.; Unida, V.; Iacovelli, F.; Manetto, A.; Kjems, J.; Desideri, A.; Biocca, S. Cellular Uptake of Covalent and Non-Covalent DNA Nanostructures with Different Sizes and Geometries. *Nanoscale* **2019**, *11* (22), 10808−10818.
(73) Kratochwil, N. A.; Huber, W.; Müller, F.; Kansy, M.; Gerber, P. R. Predicting Plasma Protein Binding of Drugs: A New Approach. *Biochem. Pharmacol.* **2002**, *64* (9), 1355−1374.
(74) Spada, A.; Emami, J.; Tuszynski, J. A.; Lavasanifar, A. The Uniqueness of Albumin as a Carrier in Nanodrug Delivery. *Mol. Pharmaceutics* **2021**, *18* (5), 1862−1894.
(75) Satya Prakash, S. Human Serum Albumin Nanoparticles as an Efficient Noscapine Drug Delivery System for Potential Use in Breast Cancer: Preparation and in Vitro Analysis. *Int. J. Nanomedicine* **2010**, *5*, 525−532.
(76) Surana, S.; Shenoy, A. R.; Krishnan, Y. Designing DNA Nanodevices for Compatibility with the Immune System of Higher Organisms. *Nat. Nanotechnol.* **2015**, *10* (9), 741−747.
(77) Rahimizadeh, P.; Yang, S.; Lim, S. I. Albumin: An Emerging Opportunity in Drug Delivery. *Biotechnol. Bioprocess Eng.* **2020**, *25* (6), 985−995.
(78) Larsen, M. T.; Kuhlmann, M.; Hvam, M. L.; Howard, K. A. Albumin-Based Drug Delivery: Harnessing Nature to Cure Disease. *Mol. Cell. Ther.* **2016**, *4*, 3.
(79) Prajapati, R.; Somoza, Á. Albumin Nanostructures for Nucleic Acid Delivery in Cancer: Current Trend, Emerging Issues, and Possible Solutions. *Cancers* **2021**, *13* (14), 3454.
(80) Karimi, M.; Bahrami, S.; Ravari, S. B.; Zangabad, P. S.; Mirshekari, H.; Bozorgomid, M.; Shahreza, S.; Sori, M.; Hamblin, M. R. Albumin Nanostructures as Advanced Drug Delivery Systems. *Expert Opin. Drug Delivery* **2016**, *13* (11), 1609−1623.
(81) Röcker, C.; Pötzl, M.; Zhang, F.; Parak, W. J.; Nienhaus, G. U. A Quantitative Fluorescence Study of Protein Monolayer Formation on Colloidal Nanoparticles. *Nat. Nanotechnol.* **2009**, *4* (9), 577−580.
(82) Choi, J.-K.; Ho, J.; Curry, S.; Qin, D.; Bittman, R.; Hamilton, J. A. Interactions of Very Long-Chain Saturated Fatty Acids with Serum Albumin. *J. Lipid Res.* **2002**, *43* (7), 1000−1010.
(83) Curry, S.; Brick, P.; Franks, N. P. Fatty Acid Binding to Human Serum Albumin: New Insights from Crystallographic Studies. *Biochimica et Biophysica Acta (BBA) - Molecular and Cell Biology of Lipids* **1999**, *1441* (2), 131−140.
(84) Curry, S.; Mandelkow, H.; Brick, P.; Franks, N. Crystal Structure of Human Serum Albumin Complexed with Fatty Acid Reveals an Asymmetric Distribution of Binding Sites. *Nat. Struct Mol. Biol.* **1998**, *5* (9), 827−835.
(85) Simard, J. R.; Zunszain, P. A.; Hamilton, J. A.; Curry, S. Location of High and Low Affinity Fatty Acid Binding Sites on Human Serum Albumin Revealed by NMR Drug-Competition Analysis. *J. Mol. Biol.* **2006**, *361* (2), 336−351.
(86) Neira, J. L.; Correa, J.; Rizzuti, B.; Santofimia-Castaño, P.; Abian, O.; Velázquez-Campoy, A.; Fernandez-Megia, E.; Iovanna, J. L. Dendrimers as Competitors of Protein−Protein Interactions of the Intrinsically Disordered Nuclear Chromatin Protein NUPR1. *Biomacromolecules* **2019**, *20* (7), 2567−2576.
(87) Sharma, R.; Raduly, Z.; Miskei, M.; Fuxreiter, M. Fuzzy Complexes: Specific Binding without Complete Folding. *FEBS Lett.* **2015**, *589*, 2533−2542.
(88) Giri, J.; Diallo, M. S.; Simpson, A. J.; Liu, Y.; Goddard, W. A.; Kumar, R.; Woods, G. C. Interactions of Poly(Amidoamine) Dendrimers with Human Serum Albumin: Binding Constants and Mechanisms. *ACS Nano* **2011**, *5* (5), 3456−3468.
(89) Wang, B.; Sun, Y.; Davis, T. P.; Ke, P. C.; Wu, Y.; Ding, F. Understanding Effects of PAMAM Dendrimer Size and Surface Chemistry on Serum Protein Binding with Discrete Molecular Dynamics Simulations. *ACS Sustainable Chem. Eng.* **2018**, *6* (9), 11704−11715.
(90) Dore, M. D.; Trinh, T.; Zorman, M.; de Rochambeau, D.; Platnich, C. M.; Xu, P.; Luo, X.; Remington, J. M.; Toader, V.; Cosa, G.; Li, J.; Sleiman, H. F. Thermosetting Supramolecular Polymerization of Compartmentalized DNA Fibers with Stereo Sequence and Length Control. *Chem.* **2021**, *7* (9), 2395−2414.
(91) Chidchob, P.; Offenbartl-Stiegert, D.; McCarthy, D.; Luo, X.; Li, J.; Howorka, S.; Sleiman, H. F. Spatial Presentation of Cholesterol Units on a DNA Cube as a Determinant of Membrane Protein-Mimicking Functions. *J. Am. Chem. Soc.* **2019**, *141* (2), 1100−1108.
(92) Trinh, T.; Liao, C.; Toader, V.; Barłóg, M.; Bazzi, H. S.; Li, J.; Sleiman, H. F. DNA-Imprinted Polymer Nanoparticles with Monodispersity and Prescribed DNA-Strand Patterns. *Nat. Chem.* **2018**, *10* (2), 184−192.
(93) Trinh, T.; Saliba, D.; Liao, C.; de Rochambeau, D.; Prinzen, A. L.; Li, J.; Sleiman, H. F. Printing" DNA Strand Patterns on Small Molecules with Control of Valency, Directionality, and Sequence. *Angew. Chem., Int. Ed.* **2019**, *58* (10), 3042−3047.
(94) Roos, K.; Wu, C.; Damm, W.; Reboul, M.; Stevenson, J. M.; Lu, C.; Dahlgren, M. K.; Mondal, S.; Chen, W.; Wang, L.; Abel, R.; Friesner, R. A.; Harder, E. D. OPLS3e: Extending Force Field Coverage for Drug-Like Small Molecules. *J. Chem. Theory Comput.* **2019**, *15* (3), 1863−1874.
(95) Harder, E.; Damm, W.; Maple, J.; Wu, C.; Reboul, M.; Xiang, J. Y.; Wang, L.; Lupyan, D.; Dahlgren, M. K.; Knight, J. L.; Kaus, J. W.; Cerutti, D. S.; Krilov, G.; Jorgensen, W. L.; Abel, R.; Friesner, R. A. OPLS3: A Force Field Providing Broad Coverage of Drug-like Small Molecules and Proteins. *J. Chem. Theory Comput.* **2016**, *12*, 281−296.
(96) Scherer, M. K.; Trendelkamp-Schroer, B.; Paul, F.; Pérez-Hernández, G.; Hoffmann, M.; Plattner, N.; Wehmeyer, C.; Prinz, J.-H.; Noé, F. PyEMMA 2: A Software Package for Estimation, Validation, and Analysis of Markov Models. *J. Chem. Theory Comput.* **2015**, *11* (11), 5525−5542.

https://doi.org/10.1021/acs.jctc.3c00720
J. Chem. Theory Comput. 2023, 19, 7873−7881